Planetary and Space Science 169 (2019) 78–85

Contents lists available at ScienceDirect

Planetary and Space Science

journal homepage: www.elsevier.com/locate/pss

A comparative study of size frequency distributions of Jupiter Trojans, Hildas and main belt asteroids: A clue to planet migration history

Fumi Yoshida [a,*], Tsuyoshi Terai [b], Takashi Ito [c], Keiji Ohtsuki [d], Patryk Sofia Lykawka [e], Takahiro Hiroi [f], Naruhisa Takato [b]

[a] Planetary Exploration Research Center, Chiba Institute of Technology, 2–17–1 Tsudanuma, Narashino, Chiba, 275–0016, Japan
[b] Subaru Telescope, National Astronomical Observatory of Japan, 650 North A'ohoku Place, Hilo, HI 96720, USA
[c] Center for Computational Astrophysics, National Astronomical Observatory of Japan, 2–21–1 Osawa, Mitaka, Tokyo, 181–8588, Japan
[d] Department of Planetology, Graduate School of Science, Kobe University, Kobe, 657–8501, Japan
[e] Kindai University, 3–4–1 Kowakae, Higashiosaka City, Osaka, 577–8502, Japan
[f] Department of Geological Sciences, Brown University, Providence, RI, 02912, USA

ARTICLE INFO

Keywords:
Asteroids
Jupiter Trojans
Surveys
Size frequency distribution
Planet formation
Solar system

ABSTRACT

Since 2002, we have obtained size frequency distributions (SFDs) of main belt asteroids (MBAs), Hildas, and Jupiter Trojans (JTs) by using the 8.2-m Subaru Telescope equipped with the wide-field CCD cameras: Suprime-Cam (SC) or Hyper Suprime-Cam (HSC). After combining these SFDs with SFDs obtained from other surveys, we performed a comparative study of SFDs for each group of small bodies in an attempt to obtain clues about planet migration that affected those populations. The large aperture of the Subaru Telescope and the wide field of view of SC or HSC allowed us to detect small moving objects up to apparent magnitudes 24.4–24.5 mag (R_c-band), which corresponds to sub–km in diameter (D) for MBAs and about 1 km for Hildas and JTs. We combined the SFDs obtained from our surveys with those derived from published data to obtain the individual representative SFD for MBAs, Hildas and JTs in the size range of sub–km to 1000 km. We found that the SFDs of JTs and Hildas are roughly flat in the R-plot while that of MBAs has a wavy structure. We also investigated the SFDs of MBAs in the inner, middle, and outer regions of the main belt. We found that the shape of the SFDs changes gradually with increasing heliocentric distance across these regions. This trend continues beyond the outer region, where the SFD becomes flatter as shown by the SFDs of JTs and Hildas. Recent planet migration models suggest that the current JTs originated in the trans-Neptunian region and were captured as Trojans during planet migration. The finding of a gradual change of the SFDs from the inner MBAs to JTs is in line with the idea that trans-Neptunian objects (TNOs) were implanted not only into the JT region, but also into the main belt outer region (including the Hildas) at the early solar system.

In order to investigate this implantation hypothesis, we considered a synthetic population of TNOs assuming with a SFD represented by a power-law distribution of $N(>D) \propto D^{-3}$, (estimated from crater record on Pluto and Charon). We then added this synthetic population to the MBA populations in various proportions. We found that the higher the proportion, the flatter the wavy SFD of MBAs becomes. This simple model yields a rough explanation for the gradual change of SFDs found from the inner main belt to the JT region. However, the shape of the modelled SFDs does not match observations for all sizes. In particular, because important discrepancies are seen in the small size range, we need to consider the removal of small objects by collisional evolution and/or Yarkovsky effect in the future.

1. Introduction

Recent theoretical models predict that there were two stages in which planetesimals experienced significant radial mixing due to migration of the giant planets (e.g. Nesvorný, 2018), in spite of the very long-term stability of the planetary motion (e.g. Ito and Tanikawa, 2002; Batygin and Laughlin, 2008) after these events. The first stage took place when Jupiter and Saturn wandered in-and-out due to interactions with the protoplanetary disk gas (Walsh et al., 2011), while the second one is represented by the time all giant planets migrated into their current

* Corresponding author.
E-mail address: fumi.yoshida@perc.it-chiba.ac.jp (F. Yoshida).

https://doi.org/10.1016/j.pss.2019.02.003
Received 22 November 2017; Received in revised form 19 December 2018; Accepted 4 February 2019
Available online 19 February 2019

orbits about 3.8–4.1 Gyr ago (the so-called Late Heavy Bombardment (LHB) period; Gomes et al. 2005; Bottke et al. 2012). According to these models, the main belt asteroids (MBAs) would consist of many kinds of objects (e.g., dry, aqueously altered, or icy bodies) reflecting their birth locations and subsequent radial mixing, while Jupiter Trojans (JTs) would consist of trans-Neptunian objects captured into the Trojan clouds during the LHB (Morbidelli et al., 2005). Although these models successfully explain various characteristics of the current Solar System, more detailed comparison with observations is desirable to critically constrain previous and potentially new models. The gradation of taxonomic types of MBAs compiled by DeMeo and Carry (2013, 2014) suggests that various kinds of small bodies were mixed up in the main belt. Such a variety in taxonomic and orbital types of the main belt objects is reflected on the diversity of the near-Earth asteroids whose dynamical origin lies largely in the main belt (e.g. Bottke et al., 2002; Stuart and Binzel, 2004; Ito and Malhotra, 2010). Also, some main belt comets (MBCs, also called active asteroids) show a periodical activity immediately after the passage of their perihelion. Such activity would be caused by sublimation of volatile material due to thermal change near the Sun. The existence of such MBCs suggests that there are a significant fraction of icy objects in the main belt.

Photometric observations can be used to determine color/taxonomic (=spectroscopic) type classification and to obtain size frequency distribution (SFD) for each group of small bodies. Such population properties and SFDs represent useful parameters in the study of radial mixing of small bodies in the early Solar System. Since colors and spectroscopic types reflect the surface composition of asteroids, they would provide information on the location where these objects formed. However, because the radial mixing caused by planet migration occurred a long time ago, the original properties of most of asteroids' surfaces were likely completely altered by space weathering. Therefore, in order to use colors and spectroscopic types as a probe to better understand this radial mixing, we need precise knowledge about the details of space weathering for each type of asteroids. Currently, we have enough knowledge about space weathering for S-type asteroids (Sasaki et al., 2001; Clark et al., 2002), but not for C-type asteroids. Moreover, laboratory experiments indicate that the spectral slope would depend on grain size in the regolith covering the asteroid surfaces (Hiroi et al., 1994, 2013; Matsuoka et al., 2015). The grain size also turned out to have a profound influence on polarimetric properties of asteroids (e.g. Belskaya et al., 2017; Ito et al., 2018). Therefore, clearly more investigations are necessary to clarify what processes mostly determine the current surface colors, textures, and spectroscopic types of MBAs. Such investigations will help us understand how these physical properties have been modified over the history of the solar system. On the other hand, colors (spectra and textures) of asteroids after their formation in the early solar system are poorly constrained, so it is difficult to know the differences of initial and currently observed colors. Therefore, it is insufficient to rely just on surface color, taxonomy, or texture when addressing the radial mixing of small bodies in early solar system.

Here, we focus on the SFDs of solar system small body populations to better understand the nature of radial mixing that these bodies experienced during planet migration. SFDs can be used to identify the origin of a population. In particular, the SFD is mainly determined by the formation environment and later altered by subsequent collisional evolution of the small body population in question.z Bottke et al. (2005) suggested that the SFD of MBAs quickly evolved and that the current wavy shape of the SFD is a fossil from a violent epoch of collisions experienced by the asteroids (i.e., accretion phase of proto-planets). Bottke et al. (2005) also suggested that MBAs larger than 100 km represent primordial objects and that their physical properties were determined during the accretion epoch, while smaller MBAs are byproducts of collisional evolution. By comparing the SFDs of inner MBAs, Near Earth Asteroids and impactors on Moon and Mars (based on the SFDs of their craters), Strom et al. (2005) found that inner MBAs likely created the old lunar craters formed about 3.8 Gyr ago (i.e. the LHB period). Strom et al. (2018) investigated the SFD of craters with diameter of 5–300 km in various areas of Ceres using the Dawn data. They found that the shape of the SFD is very similar to that of SFDs of the most ancient heavily cratered surfaces on the terrestrial planets. This means that the MBAs' SFD over a wide size range has not been modified significantly after the LHB period. Therefore, this suggests that each population of small bodies in the current solar system probably kept its SFD well preserved after the LHB. In this way, the SFD of each small body population was established by the timing of radial mixing that were caused by dynamical perturbations insensitive to body size. As long as we focus on the radial mixing of small bodies caused by gravitational perturbations by the giant planets, the SFD of each small body population which had been established by the timing of radial mixing is practically insensitive to dynamical environment and perturbation. Therefore, the populations of the same origin are expected to have the similar SFD just after the moment of the relocation, even if they were re-located due to perturbations by the giant planets, for example, during the LHB.

Table 1
Detection limit for each region from each survey.

Region or group	Size detection limit (km)	List of references
Inner belt	0.9	Spacewatch: Jedicke and Metcalfe (1998)
(2.0< a <2.6)	0.7	SDSS: Ivezić et al. (2001)
	0.2	SMBAS: Yoshida et al. (2003, 2011); Yoshida and Nakamura (2007)
	3.5	WISE: Masiero et al. (2011)
	10	AKARI: Usui et al. (2011)
Middle belt	1.4	Spacewatch: Jedicke and Metcalfe (1998)
(2.6< a <3.0)	0.3	SMBAS: Yoshida et al. (2003, 2011); Yoshida and Nakamura (2007)
	5.0	WISE: Masiero et al. (2011)
	15	AKARI: Usui et al. (2011)
Outer belt	2.3	Spacewatch: Jedicke and Metcalfe (1998)
(3.0< a <3.5)	2.9	SDSS: Ivezić et al. (2001)
	0.4	SMBAS: Yoshida et al. (2003, 2011); Yoshida and Nakamura (2007)
	6.3	WISE: Masiero et al. (2011)
	20	AKARI: Usui et al. (2011)
Hildas	1.5	Subaru: Terai and Yoshida (2018)
	10	WISE: Grav et al. (2012)
	30	AKARI: Usui et al. (2011)
Jupiter Trojans	2.0	Subaru: Yoshida and Terai (2017)
	7.0	UH 2.2: Jewitt et al. (2000)
	18	Known JTs (as of 2016 September)

a is semi-major axis in [au].

While, the SFD of collisional fragments (objects with diameter less than a few tens km) provides information about the responses from catastrophic disruption, such as their material strength and internal structure (O'Brien and Greenberg, 2003). The populations of fragment-sized small bodies sharing the same origin could possess the same SFD. Also, the SFD can tell us about the different levels of collisional evolution experienced for a given object composition (assuming that a size dependent mechanism has not affected significantly the population, e.g., the Yarkovsky effect). MBAs smaller than ~30 km in diameter have probably experienced significant orbital evolution due to the Yarkovsky effect, but Hildas/JTs or other small objects located farther from the Sun have not been affected much, because the solar radiation is weaker. All in all, we believe that SFDs covering a wide range of sizes is an convenient tool to examine the radial mixing of solar system populations caused by planet migration and to search for the origin of each population.

So far, we have investigated the SFDs of MBAs, Hildas, and JTs based on observations using the 8.2-m Subaru telescope equipped with wide-field CCD cameras: Suprime-Cam (SC) or Hyper Suprime-Cam (HSC) (Yoshida et al., 2003, 2011; Yoshida and Nakamura, 2004, 2005; 2007, 2008; Yoshida and Terai, 2017; Terai et al., 2013; Terai and Yoshida, 2018). The large aperture of the Subaru telescope and the wide field of view of SC or HSC allow us to detect small moving objects up to apparent

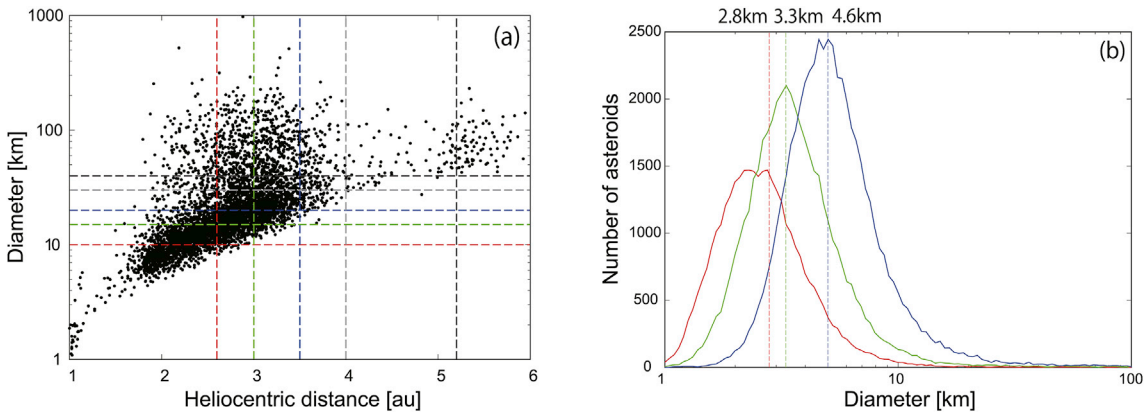

Fig. 1. (a) Heliocentric distance vs. diameter of asteroids obtained from the AKARI survey, which is reproduced from Figure 10 of Usui et al. (2011). We added lines showing the borders of inner, middle, outer belt zones, average distances of Hildas and JT populations, and the size of the detection limit for each population. (b) The differential SFD obtained by WISE (red: inner, green: middle, blue: outer belts). The dotted vertical lines show the nominal size detection limit of each region. (For interpretation of the references to color in this figure legend, the reader is referred to the Web version of this article.)

magnitudes 24.4–24.5 mag (R_c − band), which correspond to sub-km in diameter for MBAs and about 1 km for Hildas and JTs. Here, in addition to the SFDs of MBAs/Hildas/JTs obtained by several surveys using the Subaru telescope, we also consider a number of SFDs obtained from other surveys. We then combined all the SFDs and carried out a comparative study of small body populations in the Solar System based on their SFDs.

2. Collection of size frequency distributions

2.1. Main belt asteroids

We collected the MBAs' SFDs from the literature based on the Spacewatch survey (Jedicke and Metcalfe, 1998), Sloan Digital Sky Survey (SDSS; Ivezić et al., 2001), Subaru Main-belt Asteroid Survey (SMBAS; Yoshida et al., 2003; Yoshida and Nakamura, 2007; Yoshida et al., 2011), AKARI (Usui et al., 2011), and WISE (Masiero et al., 2011). See Table 1 for details. We defined the detection size range of the moving objects based on the detection limit of each survey, then truncated the population for objects smaller than the limiting size. Following the Spacewatch survey definition, we divided the main belt into three regions: inner belt ($2.0 < a < 2.6$ au), middle belt ($2.6 < a < 3.0$ au), and outer belt ($3.0 < a < 3.5$ au), where a is semi-major axis of the object.

The detection limit of the Spacewatch survey was $V \sim 21$ magnitude (Jedicke and Metcalfe, 1998). We calculated the size limit of detected objects in each main belt region assuming that the MBAs in each region have the same albedo based on the SMBAS (see below). The limiting diameters of the SFD are found to be 0.9 km, 1.4 km, and 2.3 km for the inner, middle, and outer belts, respectively.

According to Ivezić et al. (2001), the detection limit of SDSS was $r^* = 21.5$ magnitude. Ivezić et al. (2001) divided their detected MBAs into red (corresponding to S-complex) and blue (corresponding to C-complex) groups based on their colors. Then, they estimated the SFDs for red MBAs and blue MBAs separately. Since there is no information about the orbits of the detected MBAs in Ivezić et al. (2001), we could not divide the red and blue groups into the three regions of the main belt. Instead, we simply considered the red group as part of the inner belt, where S-type asteroids are dominant, and the blue group as part of the outer belt, where C-type asteroids are dominant. We did not consider the middle belt in this selection. This selection procedure might be rough, because we know that the S-type asteroids are strongly concentrated in the inner and middle belts, while the C-type asteroids are spread throughout the entire main belt. However, Ivezić et al. (2001) found that the best-fit SFD slopes for $D \lesssim 5$ km for the blue and red groups are very similar, namely 2.40 ± 0.05 and 2.20 ± 0.05, respectively. Therefore, even if we represent the SFD of the entire SDSS MBAs by the SFD of the red group, the effects on the SFD shape of each MBA population would be very small. Based on the detection limit of $r^* = 21.5$ mag and the assumed albedo of 0.16 for the red group and 0.04 for the blue group in Ivezić et al. (2001), we calculated the limiting diameters of the SFD finding 0.7 km for the red group and 2.9 km for the blue group, respectively.

The SMBAS was performed several times. The detection limit for SMBAS I, II, III was $R \sim 24.2$ mag. The detection limit of moving objects of SMBAS II was obtained in absolute magnitude (H) to be 21.25 mag, 20.61 mag and 19.95 mag for the inner, middle and outer belts, respectively (see Table 4 of Yoshida and Nakamura (2007)). In SMBAS II, Yoshida and Nakamura (2007) used the B and R_c filters and obtained the

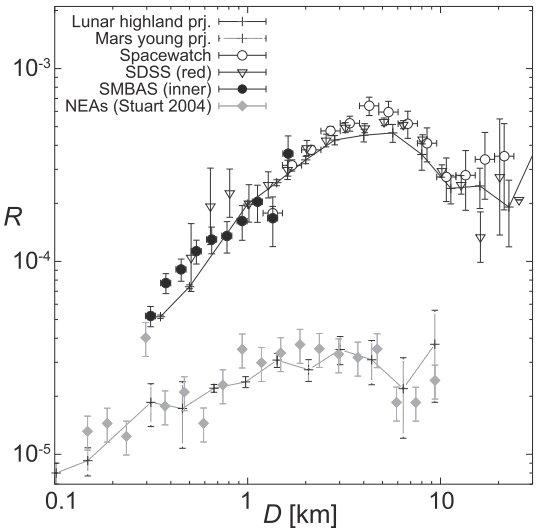

Fig. 2. Comparison of SFDs between impactors on Lunar highlands and Mars young plains, inner MBAs, and NEAs. This figure is adapted from Strom et al. (2005). The SFDs of projectiles in Lunar highlands and Mars young plains were obtained from the crater's SFDs by converting the crater sizes to projectile sizes, simulating the impact velocity of each projectile, then estimating the crater size formed by each projectile. The SFD of inner MBAs comes from asteroid surveys (Spacewatch, SDSS, SMBAS, see section 2.1). The SFD of NEAs was taken from the LINEAR survey (Stuart and Binzel, 2004). We did not include the SFD of NEAs in this comparative study. Because the NEAs's dynamical lifetime is short, their SFD would not preserve any ancient record. Many studies consider that NEAs are dynamically evolved MBAs by the influence of the Yarkovsky effect and mean motion/secular resonances with Jupiter or Saturn. Indeed, the lack of large NEAs ($D > 10$ km) may be a result of the Yarkovsky effect. If correct, we can say that the SFD of MBAs smaller than around the dip ($D = 10$–20 km shown in in Fig. 3) has likely been modified by Yarkovsky effect.

$B-R$ color of each MBA. Using the $B-R$ color, Yoshida and Nakamura (2007) divided their detected MBAs into S-like ($B-R>1.1$) and C-like ($B-R<1.1$) asteroids and calculated the ratio of the S-like and C-like asteroids (S-like/C-like ratio) for each main belt region (since the definition used in Yoshida and Nakamura (2007) is different from the S-complex and C-complex used in the SDSS (Ivezić et al., 2001), Yoshida and Nakamura (2007) used the terms of S-like and C-like asteroids). Assuming the albedo of 0.21 for the S-type and 0.06 for the C-type and using the S-like/C-like ratio obtained by Yoshida and Nakamura (2007), we calculated the mean albedo of MBAs in each main belt region (inner: 0.158, middle: 0.132, outer: 0.103). Using the mean albedo, then the limiting diameters of the SFDs were found to be 0.19 km, 0.28 km, and 0.43 km for inner, middle, and outer belts, respectively.

The AKARI survey provides diameters of asteroids. We estimate the detection limit diameter for each main belt region or a small body group (Hildas and Jupiter Trojans) from Figure 10 of Usui et al. (2011), which is the plot of heliocentric distance vs. diameter of the detected asteroids. In that figure, the asteroids are about 10 km at 2.6 au, 15 km at 3.0 au, 20 km at 3.5 au, 30 km at 4 au and 40 km at 5.2 au, respectively. This data is reproduced in Fig. 1a with additional lines indicating the lower size limits (See also Fig. 3).

The WISE (Wide-field Infrared Survey Explorer) survey also provides diameters of detected asteroids. We assumed that the limiting diameter corresponds to the smallest diameter where the slope of the cumulative SFD looks straight on the log-log plot in Figure 5 of Masiero et al. (2011). However, Joseph Masiero (private communication in 2018) kindly provided us the corresponding differential SFD, which is reproduced in Fig. 1 (b). The differential SFD allows us to find more easily where the turnover is, i.e., where the completeness begins to drop. The peaks for each differential SFD are 2.8 km, 3.3 km, and 4.6 km, in the inner, middle and outer belt, respectively. Considering the completeness of detection, we regarded the diameter of one bin larger than the peak of each region as the nominal detection limit. That is, 3.5 km, 5.0 km and 6.3 km in the inner, middle and outer belt, respectively.

The definition of the main belt range of WISE (inner: $1.8<a<2.5$ au, middle: $2.5<a<2.82$ au, and outer: $2.82<a<3.6$ au) is slightly different from that used in Spacewatch survey and SMBAS (inner: $2.0<a<2.6$ au), middle: $2.6<a<3.0$ au, and outer: $3.0<a<3.5$ au). Here, we chose the definition of Spacewatch and SMBAS, so we regarded the inner, middle, outer MBAs in WISE as the inner belt MBAs, middle belt MBAs and outer belt MBAs, respectively.

2.2. Hildas

We collected the SDF of Hildas from the data of AKARI, WISE, and the survey done by Terai and Yoshida (2018) (see Table 1). WISE detected 885 Hilda asteroids. Figures 15 and 17 of Grav et al. (2012) shows that the cumulative size distribution of Hildas has no significant slope changes till the diameter $D\sim10$ km. Therefore, the limiting diameter can be estimated to be around 10 km. Terai and Yoshida (2018) detected about 100 Hilda asteroids using the Subaru telescope equipped with the HSC and determined their SFD. The limiting diameter of Hildas' SFD is about 1.5 km in their survey, while it is 30 km in the AKARI data (assuming they are located at 4 au).

2.3. Jupiter Trojans

We collected the JTs' SFD from the surveys done by Jewitt et al. (2000) and Yoshida and Terai (2017). We also used known JTs from the MPC catalog (see Table 1).

Jewitt et al. (2000) obtained the SFD of JTs observed by the University of Hawaii 2.2 m telescope. In their Fig. 5, a discrepancy of the cumulative number of detected JTs between the raw and corrected data is clearly seen for objects fainter than $V\sim21$. We considered the detection limit of this survey to be $V\sim21$ without correction of detection efficiency. Thus, the limiting diameter of the SFD in that survey is

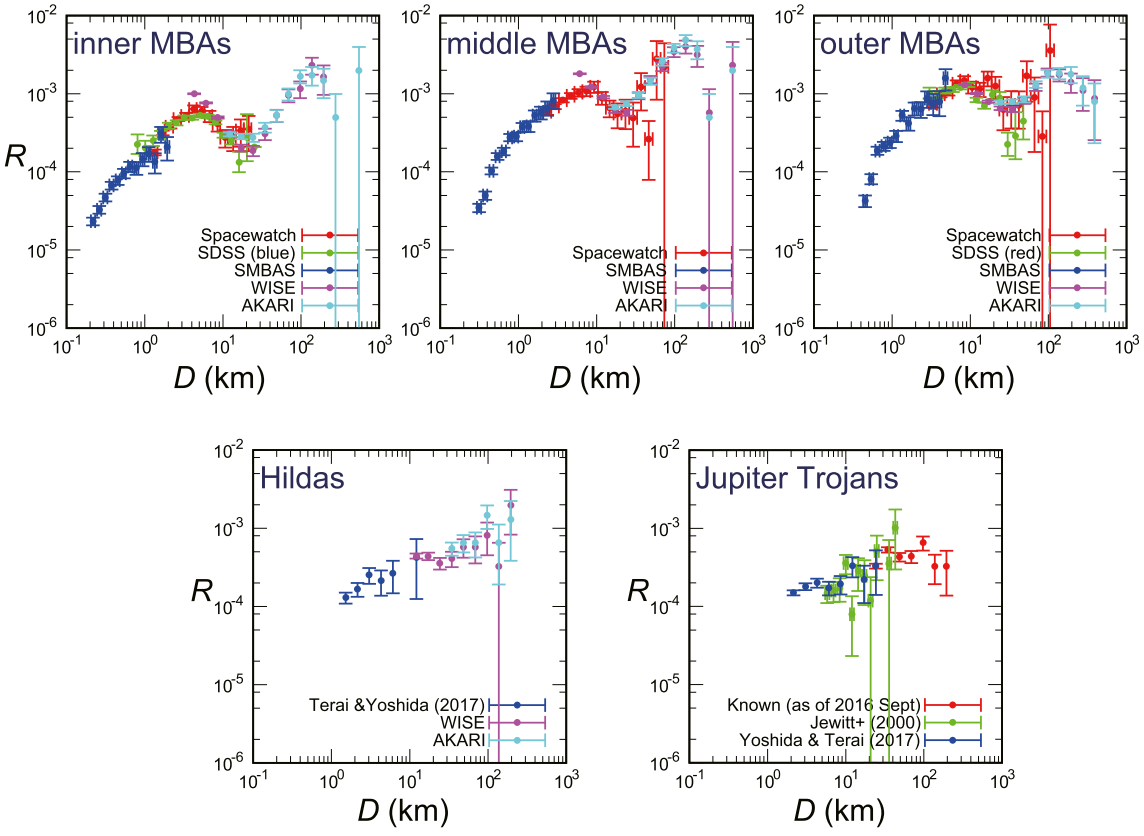

Fig. 3. *R*-curves of inner MBAs, middle MBAs, outer MBAs, Hildas, and Jupiter Trojans. The vertical and horizontal ranges are the same in all panels.

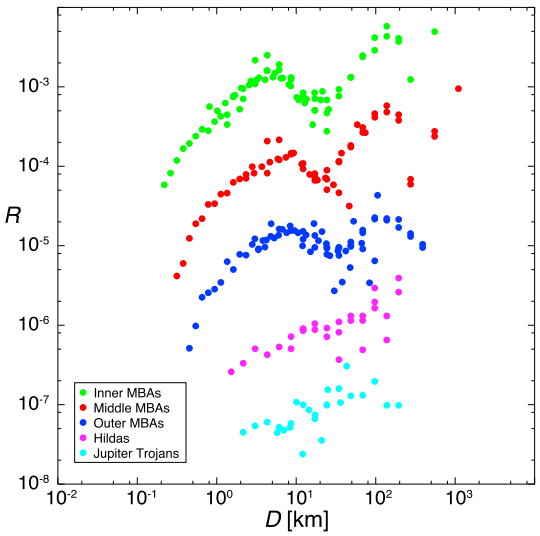

Fig. 4. *R*-curves of the five populations shown in Fig. 3 are illustrated here in a single panel. Each R-curve is vertically shifted for clarity, so that readers can better see their differences and similarities.

estimated to be 7 km assuming an albedo of 0.07 (Grav et al., 2011). Yoshida and Terai (2017) obtained the SFD of JTs observed by the Subaru telescope equipped with the HSC. The limiting diameter of the SFD is 2 km in their survey data. Szabó et al. (2007) pointed out that all JTs brighter than $H = 12.3$ mag seem to be listed in the MPC catalog. Therefore, we also included known JTs brighter than $H = 12.3$ mag in our SFD collection. Assuming an albedo of 0.07, the limiting size for the known JTs is then 18 km in diameter.

3. Comparison of size frequency distributions

We show the SFDs for each main belt region or small body group by using *R*-plots in Figs. 2 and 3. The *R*-plot was devised by the Crater Analysis techniques Working Group (Crater Analysis Techniques Working Group et al., 1979) to better illustrate the SFD of craters. When sufficient data sets are available, the *R*-plot provides a more sensitive comparison between SFDs than if using cumulative plots ($N \propto D^{-b}$).

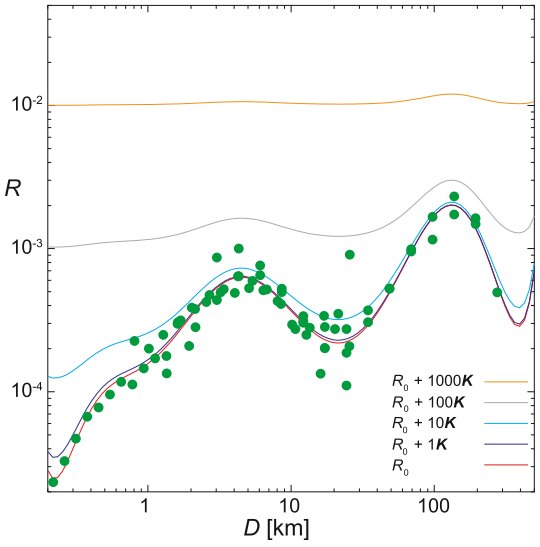

Fig. 5. *R*-curves illustrating the inner MBAs and variations after the inclusion of the $N \propto D^{-3}$. Filled circles show the SFD of the inner MBAs. The red line (R_0) represents the fitted curve for the inner MBA's SFD. See Appendix for more details. We added different fractions of the synthetic flat SFD population to the observed MBA population, as shown with different colored lines ($K = 10^{-5}$ for model convenience). One can see that the distributions get gradually flatter with the addition of larger fractions of the flat SFD population. For example, the orange curve model was added 1000 times larger flat population than the dark blue curve model. (For interpretation of the references to color in this figure legend, the reader is referred to the Web version of this article.)

Strom et al. (2005) compared the SFDs between inner MBAs, NEAs, and Lunar or Martian (northern plain) craters to identify the origin of impactors that formed these craters (see Fig. 2). Using the same methodology, we compared the SFDs between inner MBAs, middle MBAs, outer MBAs, Hildas and JTs, as shown in Figs. 3 and 4. The data for each survey were truncated at the detection limit of the survey, which was determined using the methods discussed in Section 2. The vertical *R*-values from different surveys were adjusted so that the SFDs are connected with each other smoothly.

We noticed that the SFDs of the three main belt regions present roughly similar shapes: there is a knee around $D = 100$–150 km and a dip around D=20-30 km. The similar SFD shape suggests that the entire main belt consists of a unique population that experienced the same dynamical/collisional evolution. We also noticed that the dip around D=20-30 km gets gradually shallower from the inner to the outer regions. The shape of the SFDs of Hildas and JTs looks similar: there is no significant dip or knee in their SFDs. Those SFDs appear rather flat on the *R*-plot, while the SFDs of MBAs show a wavy structure. The difference in SFDs between MBAs and Hildas/JTs and the similarity in SFDs between Hildas and JTs suggest that Hildas/JTs share the same parent population, while MBAs represent a distinct population compared to Hildas/JTs. This trend is also seen from the taxonomic type point of view. By analyzing the SDSS data, DeMeo and Carry (2014) showed that the taxonomic distribution of Hildas/JTs is clearly different from that of MBAs. Therefore, the SFDs and taxonomic distributions both suggest that the Hilda/JT populations and MBAs originated from distinct parent populations.

The gradual change of the dip depth of the SFDs from the inner MBAs to outer MBAs also drew our attention. As illustrated in Figs. 3 and 4, it is remarkable that the dip depth of the SFDs gradually flattens from the inner (MBAs) to the outer regions (Hildas/JTs). To explain these observations, we hypothesize that such a gradual change would represent different degrees of implantation of bodies captured from the trans-Neptunian region during the LHB. In particular, we propose that the SFD's dip of each main belt region, which has been established as a result of collisional evolution before the LHB, became shallower as a result of a higher fraction of implanted trans-Neptunian objects (TNOs). In other words, the dip depth would reflect the abundance of implanted TNOs, which is likely larger in the outer regions of the inner solar system. This idea is supported by the results of several solar system formation models. In fact, numerical simulations show that the gravitational interactions of giant planets with nearby planetesimals during planet migration can lead to capture of such objects into MBA, Hilda, or JT populations (Vokrouhlický et al., 2016; Morbidelli et al., 2005; Levison et al., 2009; Lykawka and Horner, 2010).

Previous observational studies are also consistent with our hypothesis. For example, Fraser et al. (2014) compared the absolute magnitude (*H*) distribution of hot and cold TNOs with that of JTs. They found that the *H* mag-distributions of JTs and hot TNOs are similar, while the cold TNOs have a distinct steeper *H*-mag distribution at the bright end. Their findings are consistent with the idea that a fraction of primordial TNOs was scattered inwards and later captured as JTs.

Studies of crater SFDs on Pluto and Charon based on New Horizons data (Singer et al., 2016; Robbins et al., 2017) further support our hypothesis. Robbins et al. (2017) found that the crater's SFD matches to a power-law size distribution with a slope of -3 within the size range 10 km $\lesssim D \lesssim$200km. Such a SFD shows a "flat" shape on the *R*-plot. Crater scaling laws allow us to estimate the size of the impactors that created the observed craters. It was found that the size of the impactors that created those craters lie within the range of 1 km $\lesssim D \lesssim$20km (Zahnle et al., 2003; Greenstreet et al., 2015). Although the SFD of TNOs smaller than $D \sim$60 km is unknown (Fraser et al., 2014), if it is the same as the SFDs of

impactors on Pluto and Charon (assuming that that SFD is also valid within the 20–60 km size range), captured small TNOs would contribute to fill the dips seen on the SFDs of MBAs in the size range of $D =$ 20–30 km.

Based on the observations discussed above, we developed a simple model to visualize the contamination of captured TNOs in *R*-plots for the populations analyzed in this paper.

Here, we made two assumptions: (1) the original SFD of the main belt region is equivalent to that of the inner MBAs and (2) the SFD of implanted TNOs during the period of the LHB is described by a power law distribution with slope -3 (i.e., a flat distribution on the $R-$plot). As discussed above, Pluto and Charon crater records provide an estimate of the SFD for the small TNO population ($D < 20$ km). Ground observations we can obtain the SFD for TNOs for larger than 60 km. In this way, there is a lack of information about the SFD of TNOs in the size range of ~ 20 km $< D < \sim 60$ km. For this reason, we cannot compare directly the SFDs of each small solar system population with that of TNOs in the same size range. Thus, we assume that the SFD of TNOs is represented by $N \propto D^{-3}$. We have added various fractions of the flat population with SFD of $N \propto D^{-3}$ to the inner MBAs, which is assumed to maintain the initial size distribution of the main belt. We then examined how the SFD changed with these additions, in particular whether the SFDs could match the currently observed SFDs from the main belt to the JT region. This idea is based on the expectation that the majority of TNOs implanted in the inner solar system consisted of smaller TNOs. This is a natural outcome, because from the SFDs we can assume that the number of small TNOs is much larger than large TNOs.

We now describe the SFD modelling and the use of *R*-plots below. The reader can find more details in the Appendix. First, we created a *R*-plot of the inner MBAs in order to add the flat SFD of the $N \propto D^{-3}$ synthetic population to the former population. Then, we systematically added the synthetic population having different fractions to the same *R*-plot. We illustrate the original SFD and the modified SFDs with these additions in Fig. 5. From this figure, it is clear that the higher the fraction of the added flat SFDs, the shallower the dips of the SFD get for the inner MBAs. Thus, the contribution of the synthetic population may explain the gradual change of SFDs in the three MBAs regions, as seen in Figs. 3 and 4. If a population with flat SFD was implanted more efficiently into the outer belt than into the inner belt, the observed gradual change could be explained by the capture of TNOs. This scenario agrees with the results from dynamical simulations (Vokrouhlický et al., 2016; Morbidelli et al., 2005; Levison et al., 2009; Lykawka and Horner, 2010).

Since the SFDs of Hildas and JTs were also likely affected in a similar way, we also investigated the influence of the flat SFD population to the former populations. Fig. 6 illustrates the SFD of each region/group plus the model generated SFD consisting of the inner belt SFD plus a certain fraction of the flat SFD population for comparisons. The parameter *K* stands for the fraction of added flat SFD population in the figure. After visual inspection, the observed SFDs roughly match the model generated SFD for each region/group. In addition, the *K* values used suggest that the Hildas and JTs need 20 times more flat SFD population objects than middle MBAs for a better fit to their current observed SFDs. The addition of the flat SFD population decreases the dip depth and the height of the peaks on the *R*-plot. It also flattens the SFD shape of smaller asteroids at ($D < 10$ km) or so. However, the observed SFD of such small asteroids is far from a flat shape. As discussed before, the discrepancy in the small size range is likely caused by the Yarkovsky effect, which is more effective on small asteroids. In addition, mean motion/secular resonances with the giant planets cause a slow leak of small MBAs ($D <$ a few km) to the NEA region (O'Brien and Greenberg, 2005). Thus, the combination of Yarkovsky and resonant effects have probably perturbed small MBAs that ultimately led to their current observed SDF shape. Because the SFD of primordial TNOs that penetrated the inner solar system likely had a flat shape on the *R*-plot in the size range $1 \lesssim D \lesssim 20$ km, these captured TNOs were also subject of the same effects aforementioned. Therefore, both the implanted population of TNOs and the primordial MBAs at sizes less than 10 20 km were preferentially removed from the main belt region.

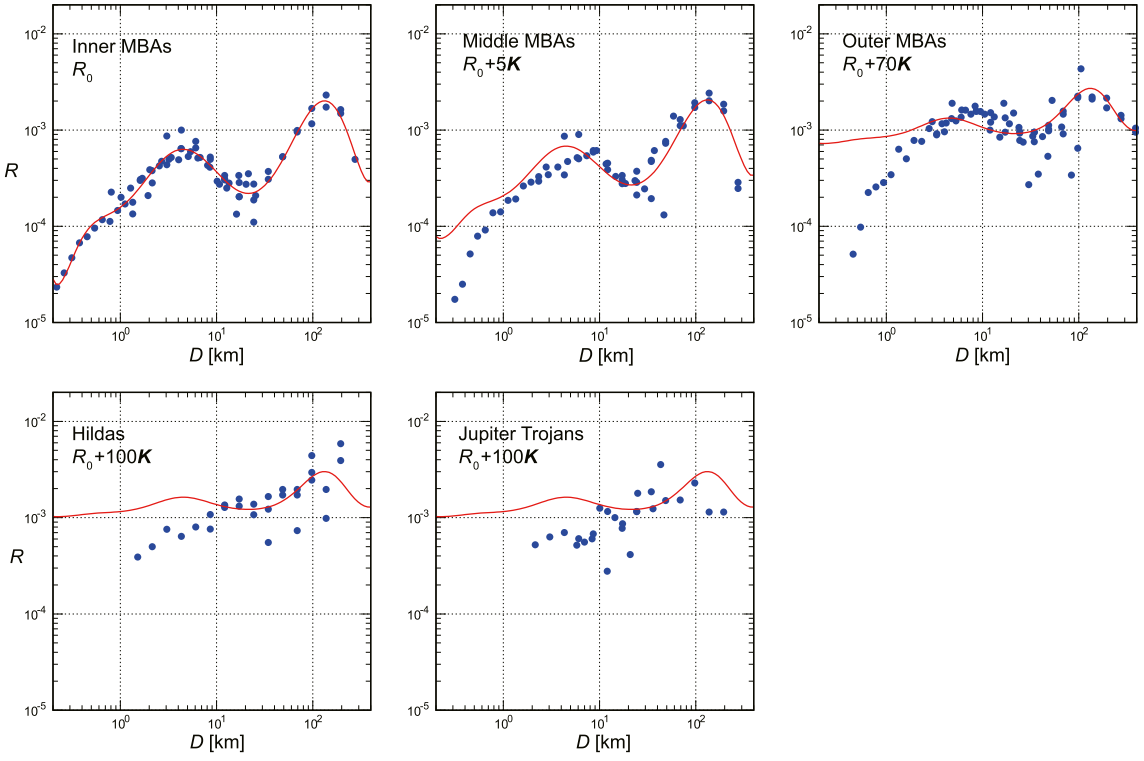

Fig. 6. Each panel shows the SFD of each region (group) along with the synthetic model of the flat (D^{-3}) SFD population that was added to the inner belt SFD. The red line in the inner MBAs panel is the same as shown in Fig. 5. In other panels, the red line indicates the best fit curve of each SFD using different fractions of the flat SFD population. (For interpretation of the references to color in this figure legend, the reader is referred to the web version of this article.)

4. Conclusion

Based on the color and absolute magnitude distributions of Hildas, JTs and TNOs, Wong & Brown (2017b, a) suggested that these populations share a common origin, as predicted by recent dynamical instability models of the Solar System. In this work, based on a comparison of SFDs of MBAs(inner, middle, outer)/Hildas/JTs/TNOs, we provide additional evidence that supports a common origin for these populations. We found that the Hildas and JTs possess a similar SFD, while their SFDs are clearly different from that of MBAs. This suggests that Hildas/JTs and MBAs did not originate from the same parent population.

We also report a gradual change of the SFD shape with increasing heliocentric distance covering the region between the inner main belt to the JT clouds. This SFD shape change was reproduced reasonably well after assuming that a trans-Neptunian population with a flat SFD (on a R-plot) was captured at different degrees across the same region. As discussed in detail in Section 3, such a flat SFD was derived from the crater SFDs of Pluto and Charon, that display a power-law distribution of index -3 over 1 km $\lesssim D \lesssim$ 20 km. The results of our simple model are summarized in Fig. 5, where the addition of the synthetic flat SFD population having different fractions roughly explains the gradual change of SFDs in the main belt. This finding provides evidence for the penetration of primordial TNOs into the inner solar system, as predicted by the dynamical models.

A caveat in our study is that the SFD of TNOs is poorly constrained. Observational studies by ground-based telescopes cannot provide the SFD for TNOs smaller than $D = 60$ km, while the crater record on Pluto and Charon provides only limited information for TNOs in the size range 1 km $\lesssim D \lesssim$ 20 km. Thus, we have no information on TNO's SFD in the size range 20 km $\lesssim D \lesssim$ 60 km. One way to fill this gap would be to investigate the crater record on the satellites of the giant planets. In particular, the crater record on the old surfaces of these satellites may constrain the SFDs of Centaurs and TNOs.

New Horizons is currently heading for 2014 MU_{69}, a TNO much smaller than Pluto and Charon. The crater record on 2014 MU_{69} could also provide useful information about the SFD of small impactors in the outer Solar System. In the near future, improved SFDs for each solar system population will be obtained by further observations of ground-based telescopes and space missions, thus allowing us to investigate the solar system history and to test theoretical models in more detail.

Acknowledgement

We gratefully acknowledge Fumihiko Usui (Kobe University, Japan) who provided us the data set from AKARI survey, and Joseph Masiero (Jet Propulsion Laboratory (JPL), Unites States) who provided us the differential SFD of MBAs from the WISE survey for producing Fig. 1 in this manuscript. We thank anonymous referees for the helpful comments that greatly improved the presentation of this manuscript. Some part of the numerical modeling and fitting were performed at Center for Computational Astrophysics (CfCA), NAOJ. This work was supported by several Japan Society for the Promotion of Science (JSPS) Kakenhi grants: JP16K05546 (F.Y.); JP18K13607 (T.T.); JP15K13604, JP25400458, JP16K05546, JP18K03730 (T.I.); JP15H03716, JP16H04041 (K.O.) and a JSPS bilateral open partnership joint research project. This study has made use of NASA's Astrophysics Data System (ADS) Bibliographic Services.

Appendix A. Supplementary data

Supplementary data to this article can be found online at https://doi.org/10.1016/j.pss.2019.02.003.

APPENDIX A. FITTING R-CURVES BY A LEAST-SQUARE METHOD

The process of producing the synthetic R-curves shown in Fig. 5 is divided into two stages. First, we fit the actual R-curve of an asteroid population by a least-square method, then we make an addition of the "flat" $N \propto D^{-3}$ population to the synthetic R-curve. As detailed below, we fit the R-curve of the inner MBAs presented in Fig. 5 using the nonlinear least-squares Marquardt–Levenberg algorithm implemented on gnuplot (http://www.gnuplot.info/). In the R-plots seen in Fig. 2 or Fig. 3, both the horizontal axis (D) and the vertical axis (R) span over a wide range, so they are expressed in logarithmic scale. Direct implementation of a least-square fit to the R data on this $\log_{10} - \log_{10}$ space would not be easy, if not impossible. Therefore we convert the original R data to a linear-scale variable through the following conversion

$$x \equiv \log_{10} D, \quad f_0(x) \equiv \log_{10} R, \tag{A1}$$

and carry out a least-square polynomial fit on the (x, y) linear space (Fig. 7a). The fitting polynomial shown in red in Fig. 7a is as follows:

$$f_0(x) = a_0 + a_1 x + a_2 x^2 + a_3 x^3 + a_4 x^4 + a_5 x^5 + a_6 x^6 + a_7 x^7 + a_8 x^8 + a_9 x^9 + a_{10} x^{10}, \tag{A2}$$

which is an output from the fit function of gnuplot. We listed the coefficients a_i $(i = 0, \cdots, 10)$ in Table 2.

Next, we convert the polynomical $f_0(x)$ defined in Eq. (A2) back to a function on the $\log_{10} - \log_{10}$ space using Eq. (A1), resulting in:

$$R = 10^{f_0(x)} = 10^{f_0(\log_{10} D)}, \tag{A3}$$

where

$$\begin{aligned} f_0(\log_{10} D) = {} & a_0 + a_1 \log_{10} D + a_2 (\log_{10} D)^2 + a_3 (\log_{10} D)^3 \\ & + a_4 (\log_{10} D)^4 + a_5 (\log_{10} D)^5 + a_6 (\log_{10} D)^6 \\ & + a_7 (\log_{10} D)^7 + a_8 (\log_{10} D)^8 + a_9 (\log_{10} D)^9 \\ & + a_{10} (\log_{10} D)^{10} \end{aligned} \tag{A4}$$

This fitting curve is shown as the blue curve in Fig. 7b on the $(D, R(D))$ plane. Naturally, the curve shape is identical to that of the red curve in Fig. 7a on the $(\log_{10} D, \log_{10} R)$ plane.

Adding a "flat" $(N \propto D^{-3})$ distribution to the fitted R is straightforward. First, $N \propto D^{-3}$ implies that R is constant independent of D. Therefore, adding

an arbitrary constant K to R and calculating $R+K$ as a function of D are the operations behind the addition of the "flat" distribution to R of a certain population. Fig. 5 is a typical representation of this procedure.

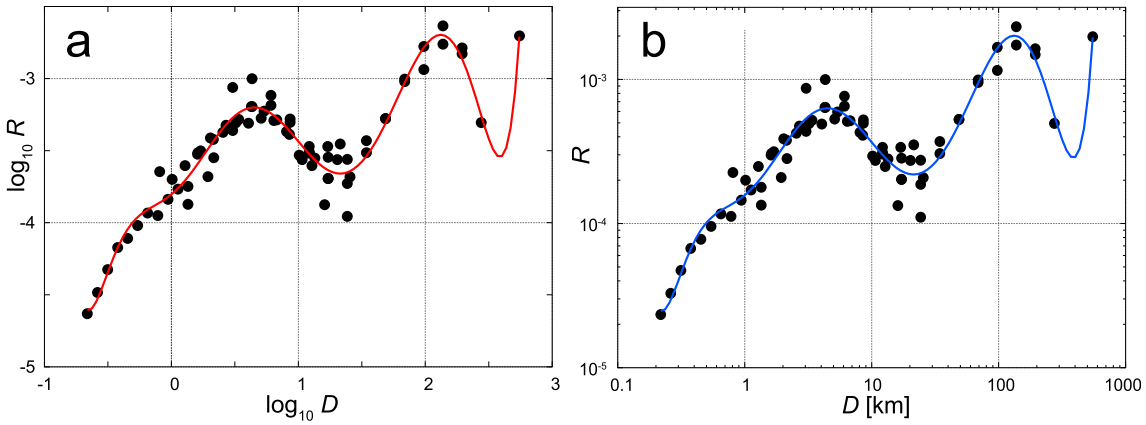

Fig. 7. The R curve of the inner MBAs drawn in two different spaces with fitting curves. a: In a linear space of $(x, f_0(x))$ or $(\log_{10}D, \log_{10}R)$. The fitting polynomial denoted in red is expressed by Eq. (A2). b: In a logarithmic space of (D, R). The inverted fitting function denoted in blue is expressed by Eq. (A3).

Table 2
The coefficients $a_i (i = 0, \cdots, 10)$ obtained through the fit function of gnuplot and used in Eqs. (A2) and (A3). Note that although each a_i is accompanied with its± error, they are not shown in the fitting curves in Fig. 7 for clarity.

a_i	value	errors
a_0	− 3.80319	±0.03461
a_1	0.733919	±0.1814
a_2	1.4095	±0.5879
a_3	1.3221	±1.091
a_4	− 7.66132	±2.832
a_5	2.36936	±2.273
a_6	7.36398	±3.436
a_7	− 8.05137	±4.592
a_8	3.60507	±2.557
a_9	− 0.795247	±0.6663
a_{10}	0.0719341	±0.06718

References

Batygin, K., Laughlin, G., 2008. Astrophys. J. 683, 1207.
Belskaya, I.N., Fornasier, S., Tozzi, G.P., et al., 2017. Icarus 284, 30.
Bottke, W.F., Durda, D.D., Nesvorný, D., et al., 2005. Icarus 175, 111.
Bottke, W.F., Morbidelli, A., Jedicke, R., et al., 2002. Icarus 156, 399.
Bottke, W.F., Vokrouhlický, D., Minton, D., et al., 2012. Nature 485, 78.
Clark, B.E., Hapke, B., Pieters, C., Britt, D., 2002. In: Bottke, W.F., Cellino, A., Paolicchi, P., Binzel, R.P. (Eds.), Asteroids III. The University of Arizona Press, Tucson, Arizona, pp. 585–599.
Crater Analysis Techniques Working Group, Arvidson, R.E., Boyce, J., et al., 1979. Icarus 37, 467.
DeMeo, F.E., Carry, B., 2013. Icarus 226, 723.
DeMeo, F.E., Carry, B., 2014. Nature 505, 629.
Fraser, W.C., Brown, M.E., Morbidelli, A., Parker, A., Batygin, K., 2014. Astrophys. J. 782, 100.
Gomes, R., Levison, H.F., Tsiganis, K., Morbidelli, A., 2005. Nature 435, 466.
Grav, T., Mainzer, A.K., Bauer, J., et al., 2011. Astrophys. J. 742, 40.
Grav, T., Mainzer, A.K., Bauer, J., et al., 2012. Astrophys. J. 744, 197.
Greenstreet, S., Gladman, B., McKinnon, W.B., 2015. Icarus 258, 267.
Hiroi, T., Pieters, C.M., Zolensky, M.E., Lipschutz, M.E., 1994. Proceedings of the NIPR Symposium on Antarctica Meteorites, vol. 7. National Institute for Polar Research, pp. 230–243.
Hiroi, T., Sasaki, S., Misu, T., Nakamura, T., 2013. In: 44th Lunar and Planetary Science Conference. Lunar and Planetary Institute), Houston, p. 1276.
Ito, T., Malhotra, R., 2010. Astron. Astrophys. 519, A63.
Ito, T., Tanikawa, K., 2002. Mon. Not. Roy. Astron. Soc. 336, 483.
Ito, T., Ishiguro, M., Arai, T., et al., 2018. Nat. Commun. 9, 2486.
Ivezić, v., Tabachnik, S., Rafikov, R., et al., 2001. Astron. J. 122, 2749.
Jedicke, R., Metcalfe, T.S., 1998. Icarus 131, 245.
Jewitt, D.C., Trujillo, C., Jane, X.L., 2000. Astron. J. 120, 1140.
Levison, H.F., Bottke, W.F., Gounelle, M., et al., 2009. Nature 460, 364.
Lykawka, P.S., Horner, J., 2010. Mon. Not. Roy. Astron. Soc. 405, 1375.
Masiero, J.R., Mainzer, A.K., Grav, T., et al., 2011. Astrophys. J. 741, 68.
Matsuoka, M., Nakamura, T., Kimura, Y., et al., 2015. Icarus 254, 135.
Morbidelli, A., Levison, H.F., Tsiganis, K., Gomes, R., 2005. Nature 435, 462.
Nesvorný, D., 2018. Annual Reviews of Astronomy and Astrophysics 56, 137.
O'Brien, D.P., Greenberg, R., 2003. Icarus 164, 334.
O'Brien, D.P., Greenberg, R., 2005. Icarus 178, 179.
Robbins, S.J., Singer, K.N., Bray, V.J., et al., 2017. Icarus 287, 187.
Sasaki, S., Nakamura, K., Hamabe, Y., Kurahashi, E., Hiroi, T., 2001. Nature 410, 555.
Singer, K.N., McKinnon, W.B., Robbins, S.J., et al., 2016. In: Lunar and Planetary Inst. Technical Report, Vol. 47, Lunar and Planetary Science Conference, p. 2310.
Strom, R.G., Malhotra, R., Ito, T., Yoshida, F., Kring, D.A., 2005. Science 309, 1847.
Strom, R.G., Marchi, S., Malhotra, R., 2018. Icarus 302, 104.
Stuart, J.S., Binzel, R.P., 2004. Icarus 170, 295.
Szabó, G.M., Ivezić, Ž., Jurić, M., Lupton, R., 2007. Mon. Not. Roy. Astron. Soc. 377, 1393.
Terai, T., Takahashi, J., Itoh, Y., 2013. Astron. J. 146, 111.
Terai, T., Yoshida, F., 2018. Astron. J. 156, 30.
Usui, F., Kuroda, D., Müller, T.G., et al., 2011. Publications of the Astronomical Society of Japan, vol. 63, p. 1117.
Vokrouhlický, D., Bottke, W.F., Nesvorný, D., 2016. Astron. J. 152, 39.
Walsh, K.J., Morbidelli, A., Raymond, S.N., O'Brien, D.P., Mandell, A.M., 2011. Nature 475, 206.
Wong, I., Brown, M.E., 2017a. Astron. J. 153, 145.
Wong, I., Brown, M.E., 2017b. Astron. J. 153, 69.
Yoshida, F., Nakamura, T., 2004. Adv. Space Sci. 33, 1543.
Yoshida, F., Nakamura, T., 2005. Astron. J. 130, 2900.
Yoshida, F., Nakamura, T., 2007. Planet. Space Sci. 55, 1113.
Yoshida, F., Nakamura, T., 2008. Publications of the Astronomical Society of Japan, vol. 60, p. 297.
Yoshida, F., Nakamura, T., Watanabe, J.-I., et al., 2003. Publications of the Astronomical Society of Japan, vol. 55, p. 701.
Yoshida, F., Terai, T., 2017. Astron. J. 154, 71.
Yoshida, F., Yagi, M., Komiyama, Y., et al., 2011. Advances in Geosciences 25, 43.
Zahnle, K., Schenk, P., Levison, H., Dones, L., 2003. Icarus 163, 263.